A hybrid control framework for impulsive control of satellite rendezvous

Mirko Brentari, Sofia Urbina, Denis Arzelier, Christophe Louembet, and Luca Zaccarian

***Abstract*—We focus on the problem of satellite rendezvous between two spacecraft in elliptic orbits. Using a linearized model of the relative dynamics, we first propose a periodic similarity transformation based on Floquet-Lyapunov theory, leading to a set of coordinates under which the free motion is linear time-invariant. Then we address the problem of impulsive control of satellite rendezvous as a hybrid dynamical system, and we show that the arising elegant representation enables designing impulsive control laws with different trade-offs between computational complexity and fuel consumption. The adopted hybrid formalism allows us to prove suitable stability properties induced by the proposed controllers. The results are comparatively illustrated on simulation examples.**

I. Introduction

Considering the increasing need for satellite servicing in space, the capability of operating an active spacecraft, the *follower* denoted by F, in close proximity of a satellite, the *leader* denoted by L, will be crucial for fulfilling complex safe space missions objectives comprising inspection, repairing, refueling, or monitoring [10]. The whole relative spacecraft maneuvering process composes what is known as the rendezvous and proximity operations, which mainly consists in getting the follower from one orbit to a box near the leader (close range rendezvous) [17], [8] and then in beginning the proximity operations required by the mission objectives. When dealing with the preliminary planning phase of space missions, it is customary to approximate actual finite-thrust powered phases of finite duration by impulsive maneuvers. The impulsive approximation for the thrust means that instantaneous velocity jumps are applied to the chaser when firing, whereas its position is continuous. This assumption, made in this paper, has proved to be very useful in reducing the complexity of guidance and control design and has been widely used in the literature dedicated to rendezvous (see [10], [7], [8] and references therein).

In this article, we are mainly interested in the proximity maneuver for which it is highly recommended to design safe impulsive maneuvers guiding the follower, from one point to a specified tolerance region in the proximity of the leader where the relative motion of the follower will be periodic and bounded. It is well known that, under Keplerian assumptions, the relative nonlinear motion between spacecraft is globally bounded [13] while the linearized relative motion equations include a secular term leading the chaser to drift away from the follower. Different conditions for the periodicity of the linearized equations of the nonlinear relative motion have been given in the literature. For instance, the authors of [1] state that the identity of the semi-major axis of the spacecraft orbits is a necessary and sufficient condition for periodicity, while Inalhan in [14] proposed a periodicity condition at perigee, for the linearized relative motion and for arbitrary eccentricity in a Cartesian and local framework. The well-known energy-matching condition, given by Gurfil in [13], involves a sixth degree polynomial equation. It is important to notice that different parametrizations (Cartesian coordinates, orbital elements) of the relative motion have been used in these previous developments.

Here we consider the parametric expression for the relative motion proposed in [7] and used to characterize in a simple way box-constrained periodic relative motions [9]. Using that parametric expression, any relative periodic trajectory is defined, in a linearized context, by 5 constant parameters. In particular, building on the result presented in [7], the contribution of the present paper is twofold. First, we propose a new coordinate transformation which leads to a simplified characterization of periodic trajectories when applied to the Tschauner-Hempel equations of the elliptic linearized relative motion. Second, three different hybrid feedback-control laws are designed by taking advantage of the particular formulation of the rendezvous problem. The use of the hybrid framework [12] for representing nonlinear hybrid dynamical systems (whose solutions exhibit continuous evolution and impulsive behavior) allows us to state and prove suitable stability properties of the proposed impulsive control laws (including, e.g., the one originally presented in [8]) when applied to the linear time-varying dynamics of the closed-loop system. This work fits well within some recent trends witnessed by spacecraft applications benefiting from hybrid systems approaches. As an example, we mention the recent invited session "A Spacecraft Benchmark Problem for Analysis & Control of Hybrid Systems" presented at the 2016 IEEE Conference on Decision and Control, where several interesting works have been presented. While none of them tackles the specific impulsive elliptic control problem addressed here, the ones most relevant with respect to our contribution are [18], where the design of multiple hybrid controllers for different phases of the rendezvous is conducted in the same hybrid control framework, and [15], where the proposed spacecraft benchmark problem could be easily extended to encompass impulsive chemical thrust as a fourth control implementation option.

Preliminary results in the directions of this work have been published in [6]. Here we make several steps forward. First, we introduce a tri-impulsive law that was not present in [6] and

M. Brentari and L. Zaccarian are with Dipartimento di Ingegneria Industriale, University of Trento, Italy

D. Arzelier, C. Louembet, S. Urbina and L. Zaccarian, LAAS-CNRS, Université de Toulouse, CNRS, France arzelier,louembet,lsurbina,zaccarian@laas.fr

Work supported in part by grant PowerLyap funded by CaRiTRo.

Work supported in part by CNES under convention 117826.

which is capable of asymptotically stabilizing the desired orbit via periodic transient motions. Second, we give statements and proofs of our stability results (those were not included in [6]). Third, we provide new and more convincing numerical illustrations of the advantages arising from the proposed strategies, which are validated on a numerical model taking into account several nonlinear effects that are disregarded in the design model. Recent efforts in a different research direction are also reported in [11], which addresses a similar impulsive control problem aiming at steering the chaser spacecraft to a forward invariant tolerance box. In that work, the attention is devoted to minimizing some cost function penalizing fuel consumption, by way of an MPC strategy. The arising solution is numerically more complex because it requires solving an on-line optimization problem. Moreover, different from this work, no stability or convergence guarantee is given in [11].

The paper is structured as follows. In Section II we propose a convenient representation of the relative dynamics, that has deep roots in the existing literature. In Section III we propose a hybrid representation of the dynamics subject to impulsive thrusts. In Section IV we propose three different control laws for the stabilization of a desired periodic orbit. Finally, in Section V we illustrate the proposed controllers on several simulation studies also involving nonlinearities neglected in the design phase. Finally, conclusions are drawn in Section VI.

Notation: a, e, ν and T are respectively the semi-major axis, the eccentricity, the true anomaly and the period of the leader's orbit. $\mu_g = 398600.4415 \times 10^9$ $\mathrm{m}^3/\mathrm{s}^2$ is the standard gravitational parameter for the Earth. f' represents the differentiation of the function f with respect to the true anomaly ν. I_n is the identity matrix of dimension n. For a set S, $\bar{S}$ denotes the closure of the set S.

II. LTI STATE-SPACE FOR THE LINEARISED RELATIVE EQUATIONS OF MOTION

A. Hybrid form of the linearized relative equations of motion

The proximity operations between two spacecraft are characterized by the use of relative navigation since the separation between spacecraft is sufficiently small. In this framework, the relative motion of the follower is described in the Local-Vertical-Local-Horizontal (LVLH) frame attached to the leader [17]. The origin of the coordinate frame is located at the center of mass of the leader and the space is spanned by $(x,\ y,\ z)$ where the z axis is in the radial direction (R-bar) oriented towards the center of the Earth, the y axis is perpendicular to the leader orbital plane and pointing in the opposite direction of the angular momentum (H-bar) while the x axis is chosen such that $x = y \times z$ (V-bar, see Figure 1).

Under Keplerian assumptions (no orbital perturbations are considered) and an elliptic reference orbit, the equations of motion for the relative motion in the LVLH frame may be linearized for close separation between the leader and the follower [2, Chapter 5, Section 5.6.1]:

$$\begin{aligned} &\dot{X} = A(t)X && \text{free motion} \\ &X^+ = X + \begin{bmatrix} 0_{3\times 3} \\ I_3 \end{bmatrix} \int_{t^-}^{t^+} \frac{f(\tau)}{m_F}\, d\tau && \begin{array}{c}\text{when applying} \\ \text{impulsive thrusts,}\end{array} \end{aligned} \tag{1}$$

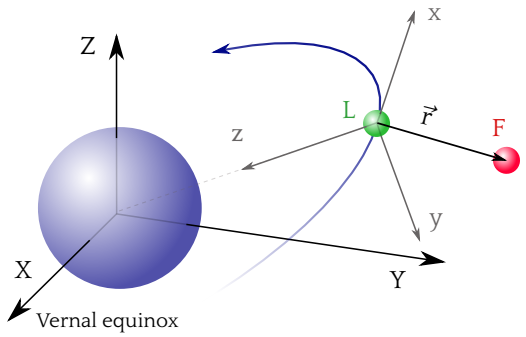

Fig. 1: LVLH frame for relative spacecraft dynamics.

where state $X = (x, y, z, dx/dt, dy/dt, dz/dt)$ represents positions and velocities in the three fundamental axes of the LVLH frame, $f(t)$ is the thrust vector, X^+ is the state vector right after the impulsive thrust, m_F, the mass of the follower, is assumed constant, and matrix $A(t)$ is a suitable periodic function of time t given by:

$$A(t) := \begin{bmatrix} 0 & 0 & 0 & 1 & 0 & 0 \\ 0 & 0 & 0 & 0 & 1 & 0 \\ 0 & 0 & 0 & 0 & 0 & 1 \\ a_1(t) & 0 & \ddot{\nu} & 0 & 0 & 2\dot{\nu} \\ 0 & a_2(t) & 0 & 0 & 0 & 0 \\ -\ddot{\nu} & 0 & a_3(t) & -2\dot{\nu} & 0 & 0 \end{bmatrix}, \tag{2}$$

where

$$\begin{aligned} a_1(t) &:= \dot{\nu}^2 + 2k^4\rho^3(\nu), \\ a_2(t) &:= \dot{\nu}^2 - k^4\rho^3(\nu), \\ a_3(t) &:= -k^4\rho^3(\nu), \end{aligned}$$

and where we recall that:

$$\dot{\nu} := \frac{d\nu}{dt} = \frac{n}{(1-e^2)^{3/2}} \underbrace{(1 + e\cos\nu)}_{\rho(\nu)}{}^2 =: k^2\rho(\nu)^2, \tag{3}$$

where $n = \sqrt{\dfrac{\mu_g}{a^3}} = 2\pi/T$ is the mean motion of the leader orbit, satisfying for any fixed ν_0, t_0,

$$\nu - \nu_0 = 2\pi \quad \Rightarrow \quad n(t - t_0) = 2\pi. \tag{4}$$

We may define the impulsive control input (essentially equivalent to velocity jumps in the three axes) as:

$$\Delta v(t_k) := \int_{t_k^-}^{t_k^+} \frac{1}{m_F} \begin{bmatrix} f_x(t) \\ f_y(t) \\ f_z(t) \end{bmatrix} dt, \tag{5}$$

which is directly associated to the fuel consumption and where t_k is a generic firing time.

In order to simplify the linearized equations (1) and (2), classical derivations dating back to the seminal publications of Lawden [16, Chapter 5] and Tschauner-Hempel [23] correspond to first applying a change of independent variable from time t to true anomaly ν, and then introducing the following coordinate change which is indeed useful for simplifying the expression of the dynamics:

$$T(\nu) := \begin{bmatrix} \rho(\nu) I_3 & 0_{3\times 3} \\ \rho(\nu)' I_3 & \rho(\nu) I_3 \end{bmatrix}, \tag{6}$$

where $\rho(\nu)' := d\rho(\nu)/d\nu$. This leads to the following hybrid

representation of the so-called Tschauner-Hempel (TH) equations with a new state $\tilde{X}(\nu)$ replacing $X(t)$:

$$\begin{aligned} \tilde{X}' &= \tilde{A}(\nu)\tilde{X} && \text{free motion,} \\ \tilde{X}^+ &= \tilde{X} + \underbrace{\frac{1}{k^4\rho(\nu)^3}\begin{bmatrix}0_{3\times3}\\ I_3\end{bmatrix}}_{=:\tilde{B}(\nu)} u && \text{when applying impulsive thrusts,} \end{aligned} \tag{7}$$

where $u = \Delta v$ represents the applied impulse, state $\tilde{X} = (\tilde{x}, \tilde{y}, \tilde{z}, d\tilde{x}/d\nu, d\tilde{y}/d\nu, d\tilde{z}/d\nu)$ represents positions and velocities with respect to ν, and

$$\tilde{A}(\nu) := \begin{bmatrix} 0 & 0 & 0 & 1 & 0 & 0 \\ 0 & 0 & 0 & 0 & 1 & 0 \\ 0 & 0 & 0 & 0 & 0 & 1 \\ 0 & 0 & 0 & 0 & 0 & 2 \\ 0 & -1 & 0 & 0 & 0 & 0 \\ 0 & 0 & \frac{3}{\rho(\nu)} & -2 & 0 & 0 \end{bmatrix}. \tag{8}$$

B. A new fundamental solution to the TH equations

In this article, we propose the two following additional transformations, the first one arising from similar observations to those in [8], and the second one arising from a Floquet-Lyapunov derivation. Although the state-space equation (7) is linear time-varying, $\tilde{A}(\nu)$ is simple enough to allow for the derivation of the autonomous solution of (7) via the computation of a fundamental matrix $\varphi_{\nu_0}(\nu)$ and a transition matrix $\tilde{\Phi}(\nu, \nu_0)$. For instance, the so-called Yamanaka-Ankersen form of this transition matrix has been proposed in [24]. Here, a new fundamental matrix is proposed, corresponding to

$$\varphi_{\nu_0}(\nu) := \begin{bmatrix} 0 & 0 & \rho^2 & -c\left(1+\frac{1}{\rho}\right) & s\left(1+\frac{1}{\rho}\right) & \rho^2 J \\ \frac{c}{\rho} & \frac{s}{\rho} & 0 & 0 & 0 & 0 \\ 0 & 0 & -e\,s & s & c & \frac{2}{3}\text{-}esJ \\ 0 & 0 & -2\,e\,s & 2s & 2c\text{-}e & 1\text{-}2esJ \\ -\frac{s}{\rho} & \frac{c}{\rho} & 0 & 0 & 0 & 0 \\ 0 & 0 & -e\,s' & s' & c' & -e\left(s'J+\frac{s}{\rho^2}\right) \end{bmatrix} \tag{9}$$

where the following shortcuts are used (with a slight abuse of notation):

$$\rho = \rho(\nu),\ s = \sin(\nu)\rho(\nu),\ c = \cos(\nu)\rho(\nu), \tag{10}$$

$$J = J(\nu, \nu_0) := \int_{\nu_0}^{\nu} \frac{1}{\rho(u)^2} du = \frac{n}{(1-e^2)^{3/2}}(t - t_0). \tag{11}$$

The 6 columns of $\varphi_{\nu_0}(\nu)$ form a basis spanning the 6-dimensional vector space of autonomous solutions of (7), since each column is indeed a solution of the autonomous equation (7), and

$$\det(\varphi_{\nu_0}(\nu)) = \frac{e^2-1}{3} \neq 0\ ,\ \forall\ e \in [0, 1)\,. \tag{12}$$

These solutions are periodic except for the secular drift term $J(\nu, \nu_0)$, which is 0 only when $\nu = \nu_0$. For this special case, we may appreciate the usefulness of the fundamental matrix in (9), which leads to defining the change of coordinates in (15), inducing the simplified free motion dynamics in (17). The state transition matrix of the LTV free motion in (7) is then easily obtained as

$$\tilde{\Phi}(\nu, \nu_0) := \varphi_{\nu_0}(\nu)\varphi_{\nu_0}(\nu_0)^{-1}. \tag{13}$$

The particular interest of considering the fundamental matrix $\varphi_{\nu_0}(\nu)$ instead of the one used in the reference [24] appears clearly in the following, when trying to obtain the simplest possible LTI expression for the relative dynamical equations (7) via a Floquet-Lyapunov similarity transformation.

C. A periodic similarity transformation

Our first objective is to characterize the periodic autonomous solutions associated to (9) by transforming $\tilde{A}(\nu)$ into a convenient sparse dynamic matrix via a well chosen similarity transformation as proposed in [7]. The similarity transformation used in this paper is slightly different from the one used in [7] and is given by:

$$\begin{aligned} \bar{\xi}(\nu) &:= \begin{bmatrix} \bar{\xi}_1(\nu) & \cdots & \bar{\xi}_6(\nu) \end{bmatrix}^T \\ &:= C(\nu)\,\tilde{X}(\nu), \end{aligned} \tag{14}$$

where $C(\nu) := \varphi_\nu(\nu)^{-1}$ can be computed explicitly and corresponds to

$$C(\nu) = \begin{bmatrix} 0 & c_\nu & 0 & 0 & -s_\nu & 0 \\ 0 & s_\nu & 0 & 0 & c_\nu & 0 \\ 1 & 0 & -\frac{3es_\nu(1+\rho)}{\rho(e^2-1)} & \frac{es_\nu(1+\rho)}{e^2-1} & 0 & \frac{\rho^2-ec_\nu-3}{e^2-1} \\ e & 0 & -3s_\nu & s_\nu(1+\rho) & 0 & c_\nu\rho \\ 0 & 0 & \frac{3(c_\nu+e)}{e^2-1} & -\frac{c_\nu(1+\rho)+e}{e^2-1} & 0 & \frac{s_\nu\rho}{e^2-1} \\ 0 & 0 & -\frac{3(3ec_\nu+e^2+2)}{e^2-1} & \frac{3\rho^2}{e^2-1} & 0 & -\frac{3es_\nu\rho}{e^2-1} \end{bmatrix}, \tag{15}$$

where we used $c_\nu := \cos(\nu)$ and $s_\nu := \sin(\nu)$. We emphasize that the states in (14) is one among the infinitely many possible combinations of the constants appearing in the analytical solutions of [16, Chapter 5] and [23]. Alternative combinations have appeared in the literature, including those in [7] and those in [21]. For instance, we get the following linear relation between the set of constants used in the reference [21] (and therein denoted by the symbol c) and the vector of constants $\bar{\xi}$ used herein.

$$\bar{\xi} = \begin{bmatrix} 0 & 0 & 0 & 0 & -1 & 0 \\ 0 & 0 & 0 & 0 & 0 & -1 \\ 0 & 0 & 3J/(e^2-1) & 1 & 0 & 0 \\ 0 & -1 & 0 & e & 0 & 0 \\ -1 & 0 & 0 & 0 & 0 & 0 \\ 0 & 0 & 3/(e^2-1) & 0 & 0 & 0 \end{bmatrix} \begin{bmatrix} c_1 \\ c_2 \\ c_3 \\ c_4 \\ c_5 \\ c_6 \end{bmatrix} \tag{16}$$

Note that, based on the results of [21] and the developments in [20], relation (16) may then be used to give the expression of the vector of differential orbital elements $(\delta a\ \ \delta e\ \ \delta i\ \ \delta\Omega\ \ \delta\omega\ \ \delta M_0)$ as a function of $\bar{\xi}$. Applying the periodic similarity transformation in (15) to the dynamic

matrix $\tilde{A}(\nu)$, we get:

$$\begin{aligned}\bar{A}(\nu) &:= \left[C'(\nu)C^{-1}(\nu) + C(\nu)\tilde{A}(\nu)C^{-1}(\nu)\right], \\ &= \left[\begin{array}{cc|ccc|c} 0 & 0 & 0 & 0 & 0 & 0 \\ 0 & 0 & 0 & 0 & 0 & 0 \\ \hline 0 & 0 & 0 & 0 & 0 & \rho(\nu)^{-2} \\ 0 & 0 & 0 & 0 & 0 & 0 \\ 0 & 0 & 0 & 0 & 0 & 0 \\ 0 & 0 & 0 & 0 & 0 & 0 \end{array}\right].\end{aligned} \tag{17}$$

Note that the structure of $C(\nu)$ preserves the decoupling between the motion in the leader's orbital plane (x, z) and the out-of-plane motion along y illustrated by the partitioning indicated in (17). Periodic autonomous solutions associated to (9) are characterized by constant solutions of $\bar{\xi}' = \bar{A}(\nu)\bar{\xi}$. From $\bar{A}(\nu)$, it is then possible to deduce that the states $\bar{\xi}_1$, $\bar{\xi}_2$, $\bar{\xi}_4$, $\bar{\xi}_5$ and $\bar{\xi}_6$ are constant solutions, while $\bar{\xi}_3(\nu)$ is a constant solution if and only if $\bar{\xi}_6(\nu) = 0$. This appears more clearly when computing the new state transition matrix associated to $\bar{A}(\nu)$ as:

$$\begin{aligned}\bar{\Phi}(\nu, \nu_0) &:= C(\nu)\tilde{\Phi}(\nu, \nu_0)C(\nu_0)^{-1} \\ &= \left[\begin{array}{cc|ccc|c} 1 & 0 & 0 & 0 & 0 & 0 \\ 0 & 1 & 0 & 0 & 0 & 0 \\ \hline 0 & 0 & 1 & 0 & 0 & J(\nu, \nu_0) \\ 0 & 0 & 0 & 1 & 0 & 0 \\ 0 & 0 & 0 & 0 & 1 & 0 \\ 0 & 0 & 0 & 0 & 0 & 1 \end{array}\right].\end{aligned} \tag{18}$$

D. A Floquet-Lyapunov similarity transformation

Since the dynamic matrix $\bar{A}(\nu)$ is periodic of period 2π, the next step consists in the application of Floquet-Lyapunov theory, as in [7] and [22], and to look for a periodic similarity transformation matrix $S(\nu)$, transforming the original *LTV* dynamical system into an equivalent *LTI* dynamical system, namely:

$$\widehat{\bar{\xi}}(\nu) := S(\nu)\bar{\xi}(\nu) \ , \tag{19}$$

$$\widehat{\bar{\xi}}\,'(\nu) = \widehat{A}\,\widehat{\bar{\xi}}(\nu) \ , \tag{20}$$

where $\widehat{A}$ is a matrix independent of ν. We know that, given $S(\nu)$, $\widehat{A}$ is given by:

$$\widehat{A} := S'(\nu)S^{-1}(\nu) + S(\nu)\bar{A}(\nu)S^{-1}(\nu) \ . \tag{21}$$

Via a right multiplication of (21) by $S(\nu)$, we obtain the differential equation:

$$S'(\nu) = \widehat{A}S(\nu) - S(\nu)\bar{A}(\nu) \ . \tag{22}$$

Equation (22) represents a matrix differential equation whose solution is given in equation (23) and comes from Floquet Theory [4]. Therefore,

$$S(\nu) = \mathrm{e}^{\widehat{A}(\nu - \nu_f)}S(\nu_f)\bar{\Phi}(\nu_f, \nu) \ , \tag{23}$$

where $\nu_f \in [0, 2\pi]$ (f stands for Floquet) is an arbitrary parameter. Imposing the periodicity condition on $S(\nu)$ with $\nu = \nu_f + 2\pi$ in (23) gives:

$$S(\nu_f + 2\pi) = S(\nu_f) = \mathrm{e}^{2\pi\widehat{A}}S(\nu_f)\bar{\Phi}(\nu_f, \nu_f + 2\pi). \tag{24}$$

From (24) we get:

$$S(\nu_f) = \mathrm{e}^{2\pi\widehat{A}}S(\nu_f)\bar{\Psi}(\nu_f)^{-1} \ , \tag{25}$$

where $\bar{\Psi}(\nu_f) = \bar{\Phi}(\nu_f + 2\pi, \nu_f)$ is the monodromy matrix (state transition matrix over one period) of $\bar{A}(\nu)$. Denoting by T the leader's orbital period, we have:

$$J(\nu_f + 2\pi, \nu_f) = \frac{n}{(1 - e^2)^{3/2}}T = \frac{2\pi}{(1 - e^2)^{3/2}}. \tag{26}$$

Using (11) and (18), the monodromy matrix $\bar{\Psi}(\nu_f)$ is therefore given by:

$$\bar{\Psi}(\nu_f) = \left[\begin{array}{cc|ccc|c} 1 & 0 & 0 & 0 & 0 & 0 \\ 0 & 1 & 0 & 0 & 0 & 0 \\ \hline 0 & 0 & 1 & 0 & 0 & \dfrac{2\pi}{(1 - e^2)^{3/2}} \\ 0 & 0 & 0 & 1 & 0 & 0 \\ 0 & 0 & 0 & 0 & 1 & 0 \\ 0 & 0 & 0 & 0 & 0 & 1 \end{array}\right]. \tag{27}$$

In solving (23) under constraint (25), we look for a solution having the same structure as $\bar{A}(\nu)$ in (17), namely satisfying $\widehat{A}^2 = 0$, which gives:

$$\mathrm{e}^{\widehat{A}\nu} = \sum_{k=1}^{\infty} \frac{\nu^k}{k!}\widehat{A}^k = I + \nu\widehat{A}. \tag{28}$$

Equation (25) becomes:

$$S(\nu_f)\bar{\Psi}(\nu_f) = (I + 2\pi\widehat{A})S(\nu_f) \ , \tag{29}$$

or equivalently:

$$2\pi\widehat{A} = S(\nu_f)\bar{\Psi}(\nu_f)S(\nu_f)^{-1} - I \ , \tag{30}$$

where $S(\nu_f)$ is an arbitrary matrix parameter. Here we select $S(\nu_f)$ as the identity matrix, to get

$$\widehat{A} = \left[\begin{array}{cc|ccc|c} 0 & 0 & 0 & 0 & 0 & 0 \\ 0 & 0 & 0 & 0 & 0 & 0 \\ \hline 0 & 0 & 0 & 0 & 0 & (1 - e^2)^{-3/2} \\ 0 & 0 & 0 & 0 & 0 & 0 \\ 0 & 0 & 0 & 0 & 0 & 0 \\ 0 & 0 & 0 & 0 & 0 & 0 \end{array}\right]. \tag{31}$$

The Floquet-Lyapunov similarity transformation is finally computed from equation (23) as:

$$\begin{aligned}S(\nu) &= \left(I + (\nu - \nu_f)S(\nu_f)\widehat{A}\right)\bar{\Phi}(\nu_f, \nu) \\ &= \left[\begin{array}{cc|ccc|c} 1 & 0 & 0 & 0 & 0 & 0 \\ 0 & 1 & 0 & 0 & 0 & 0 \\ \hline 0 & 0 & 1 & 0 & 0 & \dfrac{\sigma(\nu)}{(1 - e^2)^{3/2}} \\ 0 & 0 & 0 & 1 & 0 & 0 \\ 0 & 0 & 0 & 0 & 1 & 0 \\ 0 & 0 & 0 & 0 & 0 & 1 \end{array}\right],\end{aligned} \tag{32}$$

where we introduced the function:

$$\begin{aligned}\sigma(\nu) :=& (\nu - \tilde{\nu}) - n(t - \tilde{t}) \\ =& (\nu - \tilde{\nu}) - (M - \tilde{M}) \\ =& \Delta\nu - \Delta M,\end{aligned} \tag{33}$$

based on an arbitrary true anomaly value $\tilde{\nu}$ (in our simulations we select $\tilde{\nu} = 0$) corresponding to a specific time value $\tilde{t}$ (in

our simulations we select $\tilde{t} = 0$). Function σ in (33) is clearly periodic and bounded, due to the geometric dependence of ν and M when the leader follows a Keplerian elliptic motion.

The following result establishes a first contribution of this paper showing that dynamics (7) can be transformed to a convenient linear time-invariant form by exploiting transformations (6), (15), and (32). The proof of the lemma is omitted as it follows from the mathematical derivations discussed above, and from periodicity of matrices C and S.

Lemma 1: Consider matrices in (15) and (32). Then the following operation:

$$\widehat{\xi} := R(\nu)\tilde{X} := S(\nu)\, C(\nu)\tilde{X}\ , \tag{34}$$

is a linear time-varying coordinate change, namely $R(\nu)$ is invertible for all ν and R and R^{-1} are uniformly bounded. Moreover, R is periodic and transforms $\tilde{A}(\nu)$ into the following time-invariant form:

$$\begin{aligned} \widehat{A} \ &:= \ R'(\nu)R^{-1}(\nu) + R(\nu)\tilde{A}(\nu)R^{-1}(\nu) \\ &= \ \left[\begin{array}{ccc|ccc} 0 & 0 & | & 0 & 0 & 0 \\ 0 & 0 & | & 0 & 0 & 0 \\ \hline 0 & 0 & | & 0 & 0 & (1-e^2)^{-3/2} \\ 0 & 0 & | & 0 & 0 & 0 \\ 0 & 0 & | & 0 & 0 & 0 \\ 0 & 0 & | & 0 & 0 & 0 \end{array}\right]. \end{aligned} \tag{35}$$

From the peculiar structure (quasi Jordan form) of the dynamic matrix $\widehat{A}$, the following result, that was already noticed for a similar coordinate changes in [8], can be proven.

Lemma 2: A solution of the original dynamics (1) is periodic during free motion if and only if it is transformed into a constant state $\widehat{\xi}$ with the last component being zero.

Proof: If the last component of $\widehat{\xi}$ is zero, then matrix $\hat{A}$ in (35) clearly implies that $\widehat{\xi}$ remains constant during flow (free motion). As a consequence, the free motion in the original coordinates X of (1) is a linear combination of the first five columns of the periodic transformation $R(\nu)$ followed by the periodic time-scale change $\nu \to t$.

Conversely, assume that the last component of $\widehat{\xi}$ is nonzero. Then during free motion that component remains constant (the last row of $\widehat{A}$ is zero) and the third component of $\widehat{\xi}$ ramps up to infinity due to the off diagonal term $(1-e^2)^{-3/2} \neq 0$ appearing in $\widehat{A}$. As a consequence $|\widehat{\xi}|$ diverges and so does also $\tilde{X}$ because $R(\nu)$ is bounded and has bounded inverse (from Lemma 1). Also X must then diverge as $t \to \infty$ because the time-scale change is periodic. ∎

Based on Lemma 2, it is convenient to represent the system in terms of the error with respect to a desired motion $\widehat{\xi}^{\,ref}$:

$$\widehat{\xi}^{\,ref} := [\widehat{\xi}_1^{\,ref}\ \widehat{\xi}_2^{\,ref}\ \widehat{\xi}_3^{\,ref}\ \widehat{\xi}_4^{\,ref}\ \widehat{\xi}_5^{\,ref}\ 0]^T, \tag{36}$$

so that one may analyze the dynamics of the mismatch vector:

$$\widehat{\varepsilon} := \widehat{\xi} - \widehat{\xi}^{\,ref} \tag{37}$$

between the coordinate $\widehat{\xi}$ in (34) and a constant reference value in (36), representing a desired target periodic motion.

III. Impulsive control of the relative dynamics

The coordinate transformation presented in Lemma 1 of the previous section is a useful means for suitably designing an impulsive control law assigning the firing times ν_k in (7) and also the corresponding selections of u at time ν_k to stabilize the periodic motions characterized in Lemma 2.

Problem 1: Given plant (1) and its equivalent form (7), design a state feedback impulsive control law selecting the firing instants ν_k, $k \in \mathbb{N}$ and the corresponding inputs $u(\nu_k)$ such that for any selection of reference (36), a suitable set wherein $\widehat{\xi} = \widehat{\xi}^{\,ref}$ is globally asymptotically stable for the closed-loop dynamics.

To solve Problem 1, in this section we will propose hybrid control laws relying on the presence of a timer τ in charge of the sequencing of the impulsive control actions. Then, using the hybrid systems notation in [12] and state $\widehat{\varepsilon} := \widehat{\xi} - \widehat{\xi}^{\,ref}$, we may write the following general dynamic description of the closed loop, enjoying the desirable property that timers ν and τ evolve in the compact set $[0, 2\pi]$ and that the flow equation for $\widehat{\varepsilon}$ is $\widehat{\varepsilon}\,' = \widehat{A}\,\widehat{\varepsilon}$, because $\widehat{A}\,\widehat{\xi}^{\,ref} = 0$:

$$\begin{cases} \widehat{\varepsilon}\,' = \widehat{A}\,\widehat{\varepsilon}, \\ \nu' = 1, \\ \tau' = -1, \end{cases} \quad (\widehat{\varepsilon}, \nu, \tau) \in \mathcal{C}, \tag{39a}$$

$$\begin{cases} \widehat{\varepsilon}^{+} = \widehat{\varepsilon}, \\ \nu^{+} = 0, \\ \tau^{+} = \tau, \end{cases} \quad (\widehat{\varepsilon}, \nu, \tau) \in \mathcal{D}_\nu, \tag{39b}$$

$$\begin{cases} \widehat{\varepsilon}^{+} = \widehat{\varepsilon} + \widehat{B}(\nu)\gamma_u\,(\widehat{\varepsilon}, \nu)\,, \\ \nu^{+} = \nu, \\ \tau^{+} = \gamma_\tau\,(\widehat{\varepsilon}, \nu)\,, \end{cases} \quad (\widehat{\varepsilon}, \nu, \tau) \in \mathcal{D}_u. \tag{39c}$$

In equation (39), the impulsive control law has been selected as a feedback controller:

$$u = \gamma_u(\widehat{\varepsilon}, \nu), \quad \tau^{+} = \gamma_\tau(\widehat{\varepsilon}, \nu). \tag{40}$$

Moreover, according to the coordinate change given in (34), and to the results of Lemma 1, matrix $\widehat{B}(\nu) = R(\nu)\tilde{B}(\nu)$, is a periodic function of ν arising from combining the similarity transformation in (34) with the input matrix in (7), and corresponds to the matrix reported in (38) at the top of page 6.

Equation (39) is a compact representation of the impulsive feedback control action as a set of dynamical constraints that solutions should satisfy for their correct evolution. In particular, using an overall state $\eta = (\widehat{\varepsilon}, \nu, \tau)$, this dynamics falls into the general class of systems studied in [12]:

$$\begin{array}{ll} \eta \in \mathcal{C}, & \dot{\eta} = F(\eta), \\ \eta \in \mathcal{D}, & \eta^{+} \in G(\eta). \end{array} \tag{41}$$

For our model, the following selections are made:

$$\mathcal{D}_\nu \ := \ \mathbb{R}^6 \times \{2\pi\} \times [0, 2\pi], \tag{42a}$$

$$\mathcal{D}_u \ := \ \mathbb{R}^6 \times [0, 2\pi] \times \{0\}, \tag{42b}$$

$$\mathcal{D} \ := \ \mathcal{D}_\nu \cup \mathcal{D}_u, \tag{42c}$$

$$\mathcal{C} \ := \ \overline{(\mathbb{R}^6 \times [0, 2\pi] \times [0, 2\pi]) \setminus \mathcal{D}}, \tag{42d}$$

which, due to (42c), is a choice that prioritizes jumps. In particular, based on (39), functions F and G in (41) are selected as:

$$F(\eta) = \begin{bmatrix} \widehat{A}\,\widehat{\xi} \\ 1 \\ -1 \end{bmatrix}; \ G(\eta) = \bigcup_{i \in \{u,\nu\} \text{ s.t. } \eta \in \mathcal{D}_i} G_i(\eta); \tag{43a}$$

$$\widehat{B}(\nu)=\frac{1}{k^2\rho^2(1-e^2)}\begin{bmatrix} 0 & -(1-e^2)\rho s_\nu & 0 \\ 0 & (1-e^2)\rho c_\nu & 0 \\ -e(1+\rho)\rho s_\nu-\dfrac{3\sigma\rho^3}{(1-e^2)^{3/2}} & 0 & \dfrac{3\sigma e\rho^2 s_\nu}{(1-e^2)^{3/2}}-\rho^3+\rho^2+2\rho \\ (1-e^2)(1+\rho)\rho s_\nu & 0 & (1-e^2)\rho^2 c_\nu \\ (1+\rho)\rho c_\nu+e\rho & 0 & -\rho^2 s_\nu \\ -3\rho^3 & 0 & 3e\rho^2 s_\nu \end{bmatrix} \tag{38}$$

$$G_\nu(\eta)=\begin{bmatrix}\widehat{\varepsilon}\\ 0\\ \tau\end{bmatrix};\ G_u(\eta)=\begin{bmatrix}\widehat{\varepsilon}+\widehat{B}(\nu)\gamma_u\left(\widehat{\varepsilon},\nu\right)\\ \nu\\ \gamma_\tau\left(\widehat{\varepsilon},\nu\right)\end{bmatrix}. \tag{43b}$$

The proposed hybrid model (39), (42) (or its equivalent compact form in (41), (42), (43)), corresponds to the following intuitive behavior of our solutions.

- Timer ν is used as an additional state to keep track of the periodic time-varying nature of the dynamics. Using the jump set in (42a) ensures that the timer is reset to zero each time it reaches the value 2π, thereby being confined [1] to the compact set $[0,2\pi]$.
- Thrusters are fired according to (39c) whenever $\eta\in\mathcal{D}_u$, namely when the timer τ crosses zero (see (42b)). Then, at each time during the evolution of the dynamics, state τ captures the information about how long we need to wait until the next impulsive control action.
- Each time an impulsive control action is triggered, the associated control law corresponds to the value of the two functions
$$\begin{aligned}&\gamma_u:\mathbb{R}^6\times[0,2\pi]\to\mathbb{R}^3,\\ &\gamma_\tau:\mathbb{R}^6\times[0,2\pi]\to[0,2\pi],\end{aligned} \tag{44}$$
the first one assigning the current selection of the impulsive input $\widehat{u}$ (based on (40)), and the second one preassigning the time to wait until the next impulsive input should be applied. Note that the range of γ_τ is bounded so that solutions will only take values of τ in the bounded set $[0,2\pi]$.

Within the proposed hybrid context, the stability goal formulated in Problem 1 is well characterized in terms of the stability properties of the bounded attractor

$$\mathcal{A}:=\{0\}\times[0,2\pi]\times[0,2\pi], \tag{45}$$

which may be analyzed using the tools of [12, Chapter 7], because selections (42), (43) satisfy the hybrid basic conditions of [12, Assumption 6.5].

IV. Control laws

In this section, we propose three different selections for the impulsive control law (40) solving Problem 1. They are comparatively illustrated on the example studies of Section V.

[1] To avoid situations where arbitrarily small noise may cause solutions to stop because they exit $\mathcal{C}\cup\mathcal{D}$, it may be useful to replace $\{2\pi\}$ by $[2\pi,2\pi+\delta]$ for any positive δ in (42a).

A. Periodic norm-minimizing control law

While formulation (39), (40) is general enough to allow for aperiodic optimized sampling, the simplest possible selection of function γ_τ in (40) is given by periodic thrusters firing, corresponding to a certain period $\bar{\nu}\in[0,2\pi]$ fixed a priori. For instance,

$$\gamma_\tau(\widehat{\varepsilon},\nu)=\bar{\nu}, \tag{46}$$

encodes the fact that each pair of consecutive jumps has a fixed angular distance of $\bar{\nu}$.

Regarding the selection of the stabilizer γ_u, to be evaluated periodically, we make here a conservative selection leading to the useful feature that after each impulse, the state $\widehat{\varepsilon}_6=\widehat{\xi}_6$ is driven to zero. Then, in light of Lemma 2, in the absence of noise the spacecraft evolves through periodic (therefore bounded) motions. In particular, the following optimal selection is chosen:

$$\begin{aligned}u^\star=\underset{u\in\mathbb{R}^3}{\arg\min}\,|\widehat{\varepsilon}^+|^2,\ \text{subject to:}\\ \widehat{\varepsilon}^{\,+}=\widehat{\varepsilon}+\widehat{B}(\nu)u,\quad \widehat{\varepsilon}_6^{\,+}=0.\end{aligned} \tag{47}$$

Due to the specific structure of matrix function $\widehat{B}(\nu)$ in (38) at the top of page 6, we may provide an explicit form of the minimizer in (47) after defining the following quantities:

$$\hat{b}_6(\nu):=\frac{1}{k^2}\begin{bmatrix}-\frac{3\rho}{1-e^2}\\ 0\\ \frac{3e\sin(\nu)}{1-e^2}\end{bmatrix},\ \hat{B}_6^\perp(\nu):=\begin{bmatrix}e\sin(\nu) & 0\\ 0 & 1\\ \rho(\nu) & 0\end{bmatrix}, \tag{48a}$$

which clearly satisfy $\hat{b}_6(\nu)^T\hat{B}_6^\perp(\nu)=0$ because matrix $\hat{B}_6^\perp(\nu)$ generates the orthogonal complement of $\hat{b}_6(\nu)$.

With these definitions in place, we may write the explicit expression of the proposed control law as:

$$\begin{aligned}\gamma_u(\widehat{\varepsilon},\nu)=u_6-\hat{B}_6^\perp(\nu)(\widehat{B}(\nu)\hat{B}_6^\perp(\nu))^{-L}(\widehat{\varepsilon}+\widehat{B}(\nu)\ u_6)\\ \text{with } u_6:=-\frac{\hat{b}_6(\nu)}{|\hat{b}_6(\nu)|^2}\widehat{\varepsilon}_6,\end{aligned} \tag{48b}$$

where $M^{-L}=(M^TM)^{-1}M^T$ denotes the left pseudo-inverse of matrix M. The effectiveness of selection (48b) is stated in the next proposition.

Proposition 1: For any value of ν, the inverses in function (48) always exist and selection (48) coincides with the minimizer in (47), namely $\gamma_u(\widehat{\varepsilon},\nu)=u^\star$.

Proof: The existence of the inverses easily follows from

the fact that

$$\det\Big((\widehat{B}(\nu)\hat{B}_6^{\perp}(\nu))^T(\widehat{B}(\nu)\hat{B}_6^{\perp}(\nu))\Big) \tag{49}$$

$$= (1-e)^2 + 2e(1+\cos(\nu)) > 0 \tag{50}$$

$$|\hat{b}_6(\nu)|^2 = \frac{9\rho^4(\rho^2+e^2\sin(\nu)^2)}{(1-e^2)^2} > 0, \tag{51}$$

which clearly indicates that the left inverse in the first line of (48b) and u_6 in the second line of (48b) can be evaluated. To show that (48) coincides with the minimizer in (47), first notice that constraint ${\widehat{\varepsilon}_6}^+ = 0$ is automatically ensured by $\hat{b}_6(\nu)^T\hat{B}_6^{\perp}(\nu) = 0$, which implies ${\widehat{\varepsilon}_6}^+ = \hat{b}_6^T(\nu)u_6 = 0$. Therefore, noting that $\hat{B}_6^{\perp}(\nu)$ is the orthogonal complement of $\hat{b}_6(\nu)$, all possible inputs guaranteeing that ${\widehat{\varepsilon}_6}^+ = 0$ are parametrized by $\widehat{v}^\star$ in:

$$u = u_6 + \hat{B}_6^{\perp}(\nu)\ v^\star. \tag{52}$$

Therefore, the solution to (47) corresponds to (52) with $\widehat{v}^\star$ being the solution to the following unconstrained least squares problem:

$$v^\star = \arg\min_{\widehat{v}} |\widehat{\varepsilon} + \widehat{B}(\nu)u_6 + \widehat{B}(\nu)\widehat{B}_6^{\perp}(\nu)\ v|^2. \tag{53}$$

Then, as is well known (see, e.g., [3, Ex.1 pg 92]), the minimizer $v^\star$ is given by:

$$v^\star = -(\widehat{B}(\nu)\hat{B}_6^{\perp}(\nu))^{-L}(\widehat{\varepsilon} + \widehat{B}(\nu)\ u_6), \tag{54}$$

which, substituted in (52), gives (48b), as to be proven. ■

Remark 1: Based on Proposition 1, a desirable property of control law (46), (48) is that, in light of Lemma 2, it instantaneously minimizes the norm of $\widehat{\varepsilon}$ constrained to the fact that the subsequent motion be periodic. Since the norm of $\hat{b}_6$ in (48a) is never zero, then clearly, equation (48b) is always well-posed and ensures that ${\widehat{\varepsilon}_6}^+ = 0$. In addition to this, instantaneously minimizing the norm of $\widehat{\varepsilon}$ also ensures the best possible decrease at the specific fixed instant of time enforced by the periodic selection. With this logic in place, we can guarantee stability of the closed-loop but not convergence. Indeed, we can guarantee non-increase of $|\widehat{\varepsilon}|$ across jumps but there is no guarantee of obtaining a strict decrease. As a result, we anticipate a slow convergence (if any) in our simulation section when using this controller. Despite this fact, the choice (46), (48) is still an interesting one because it ensures that approaching between the two satellites is performed through periodic (bounded) motions, leading to some degree of fault tolerance (in case of malfunctioning, the satellite is on a stable relative orbit). ○

The following theorem certifies that the proposed controller solves part of Problem 1.

Theorem 1: Given control law (46), (48), the attractor $\mathcal{A}$ in (45) is uniformly globally stable for the arising closed-loop dynamics with plant (39).

Proof: First notice that $|(\widehat{\varepsilon},\nu,\tau)|_{\mathcal{A}} = |\widehat{\varepsilon}|$. Recall that a generic solution $(\mu, j) \mapsto \widehat{\varepsilon}(\mu, j)$ to the hybrid dynamics has a domain $\operatorname{dom}\widehat{\varepsilon}$ parametrized by a flowing direction and by a jumping direction j (see [12, Chap. 2] for details). Here the flowing direction is represented by the amount μ of true anomaly elapsed since the initial condition, as opposed to continuous time t for a classical hybrid systems representation. We first realize that before the first impulse, all solutions evolve in free motion along the LTI flow dynamics in (39), leading to:

$$|\widehat{\varepsilon}(\mu,0)| \le |\mathrm{e}^{2\pi\widehat{A}}||\widehat{\varepsilon}(0,0)|. \tag{55}$$

Notice now that Proposition 1 ensures that $\gamma_u(\widehat{\varepsilon},\nu) = u^\star$. In particular, after the first jump the state $\widehat{\varepsilon}_6$ remains at zero for all (hybrid) times. Then during all subsequent flows, the state $\widehat{\varepsilon}$ remains constant due to the structure of $\widehat{A}$. Moreover, across jumps, the control law is the minimizer of (47), clearly satisfying $|\widehat{\varepsilon}^{\,+}| \le |\widehat{\varepsilon}|$. As a consequence, we get:

$$|\widehat{\varepsilon}(\mu,j)| \le |\exp(2\pi\widehat{A})||\widehat{\varepsilon}(0,0)|, \tag{56}$$

for all $(\mu, j) \in \operatorname{dom}\widehat{\varepsilon}$, which establishes uniform global stability. ■

B. Two-step finite-time control law

A second selection that we propose for the controller in (40) is once again periodic, thereby corresponding to selection (46) for γ_τ. However, it corresponds to a wiser selection of γ_u (in terms of envisioned fuel consumption), performed in similar ways to what is proposed in [8], by focusing on the overall effect on the state $\widehat{\varepsilon}$ of two impulses performed at a distance of $\bar{\nu}$ from one another. In particular, using straightforward computations, if two consecutive impulses u_1 and u_2 happen at times μ_1 and $\mu_2 = \mu_1 + \bar{\nu}$, we obtain, along the corresponding solution:

$$\widehat{\Phi}(-\bar{\nu})\widehat{\varepsilon}(\mu_2, j_2+1) = \tag{57}$$

$$\widehat{\varepsilon}(\mu_1,j_1) + \underbrace{\begin{bmatrix}\hat{B}(\nu_1) & \widehat{\Phi}(-\bar{\nu})\hat{B}(\nu_1+\bar{\nu})\end{bmatrix}}_{M(\nu_1,\bar{\nu}):=}\begin{bmatrix}u_1\\u_2\end{bmatrix},$$

where (μ_1, j_1) and (μ_2, j_2) denote the hybrid times before each one of the impulses, $\widehat{\Phi}(\mu) = e^{\widehat{A}\mu} = \begin{bmatrix}1&0&0&0&0&0\\0&1&0&0&0&0\\0&0&1&0&0&\mu(1-e^2)^{-3/2}\\0&0&0&1&0&0\\0&0&0&0&1&0\\0&0&0&0&0&1\end{bmatrix}$ is the state transition matrix of the (LTI) flow dynamics in (39), and $\nu_1 = \nu(\mu_1, j_1)$.

Based on relation (57), and to the end of selecting u_1, u_2 in such a way that $\widehat{\varepsilon}(\mu_2, j_2+1)$ be zero, it is important to study the invertibility properties of matrix $M(\nu,\bar{\nu})$, which is done in the following conjecture. The result of the conjecture restricts the set of possible selections of $\bar{\nu}$ in (46).

Conjecture 1: For any value of $\nu \in [0, 2\pi]$, matrix $M(\nu,\bar{\nu})$ in (57) is invertible if and only if $\bar{\nu} \neq k\pi$, $k \in \mathbb{Z}$.

In support of the conjecture, we report in Figure 2 the value of the determinant of $M(\nu,\bar{\nu})$ for different values of ν (represented by the color code) and $\bar{\nu}$ (represented by the horizontal axis). The plot corresponds to the value $e = 0.4$ and similar plots are experienced for any value of $e < 1$. Proving Conjecture 1 is challenging from a mathematical viewpoint, but is of little interest in light of the improved results reported in Section IV-C.

If Conjecture 1 holds, for any selection $\bar{\nu} \in (0, 2\pi) \setminus \{\pi\}$, Equation (57) can be inverted to compute the unique pair of inputs $u_1^\star$, $u_2^\star$ ensuring $\widehat{\varepsilon}(\mu_2, j_2+1) = 0$ (namely that the state $\widehat{\varepsilon}$ is driven to zero after two impulses separated by $\bar{\nu}$

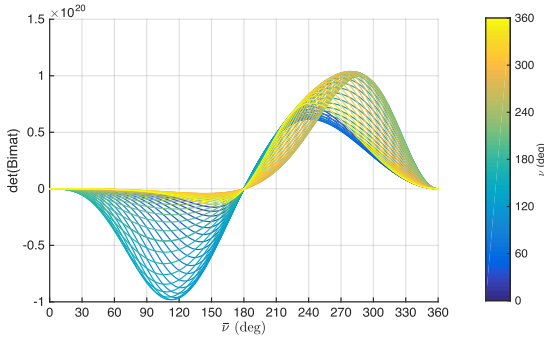

Fig. 2: Determinant of matrix $M(\nu,\bar{\nu})$ with $e=0.4$.

times). Following a receding horizon type of paradigm, we may apply the first impulse and re-evaluate the control law at the next impulse time. The above control design paradigm leads to the following selection:

$$\gamma_u(\widehat{\varepsilon},\nu) := -\left[\,I\;0\,\right] M(\nu,\bar{\nu})^{-1}\widehat{\varepsilon}, \quad \gamma_\tau(\widehat{\varepsilon},\nu)=\bar{\nu}. \tag{58}$$

The overall control strategy (46), (58) guarantees convergence to zero of the error $\widehat{\varepsilon}$ after two impulses, as established next.

Lemma 3: If $M(\nu,\bar{\nu})$ is invertible for all $\nu\in[0,2\pi]$, then selection (46), (58) guarantees that all solutions to (39) have the $\widehat{\varepsilon}$ component equal to zero after at most two jumps.

Proof: Consider two subsequent impulses associated to the control selections $u_j=\left[\,I\;0\,\right]\left[\begin{smallmatrix}u_{j,1}\\u_{j,2}\end{smallmatrix}\right]=u_{j,1}$ and $u_{j+1}=\left[\,I\;0\,\right]\left[\begin{smallmatrix}u_{j+1,1}\\u_{j+1,2}\end{smallmatrix}\right]=u_{j+1,1}$. Then, due to the property that $\left[\begin{smallmatrix}u_{j,1}\\u_{j,2}\end{smallmatrix}\right]$ brings the state to zero after two impulses, it follows that selection $\left[\begin{smallmatrix}u_{j+1,1}\\u_{j+1,2}\end{smallmatrix}\right]=\left[\begin{smallmatrix}u_{j,2}\\0\end{smallmatrix}\right]$ is a feasible one for the second impulse. As a consequence of uniqueness, arising from relation (57), this is the only possible solution and we must have $\widehat{\varepsilon}^{\,+}=0$ after the second impulse. ■

Based on Lemma 3 we can now prove that our second control law solves Problem 1 as established in the next theorem.

Theorem 2: Given $\bar{\nu}\in(0,2\pi)\setminus\{\pi\}$, assume that matrix $M(\nu,\bar{\nu})$ is invertible for any value of $\nu\in[0,2\pi]$.

Then, control law (46), (58) ensures that attractor $\mathcal{A}$ in (45) is uniformly globally asymptotically stable along the arising closed-loop dynamics with (39).

Proof: The proof is carried out by exploiting the following global version of [12, Prop. 7.5] (its proof is straightforward, taking $\mu\to\infty$ in the semiglobal version of [12, Prop. 7.5], and is actually therein implicitly used for establishing the result in [12, Ex. 7.6]).

Proposition 2: Given a nominally well-posed hybrid system $\mathcal{H}$, suppose that the compact set $\mathcal{A}$ in (45) is strongly forward invariant and globally uniformly attractive for $\mathcal{H}$. Then, it is uniformly globally asymptotically stable for $\mathcal{H}$.

To apply Proposition 2 to our case, we first notice that the data of hybrid system (39), (46), (58) satisfies the hybrid basic conditions in [12, As. 6.5], therefore, from [12, Thm 6.8], it is nominally well-posed. Concerning forward invariance of $\mathcal{A}$ (namely, all solutions starting in $\mathcal{A}$ remain in $\mathcal{A}$ for all times), it follows from the fact that the flow dynamics of $\widehat{\varepsilon}$ is linear (so the origin is an equilibrium) and the jumps guarantee non-increase of $\widehat{\varepsilon}$ (see the proof of Theorem 1). Finally, global uniform convergence is a straightforward consequence of the stronger property of uniform finite-time convergence established in Lemma 3. ■

Remark 2: A desirable feature of the established global asymptotic stability of set $\mathcal{A}$ can be obtained by the robustness characterization given in [12, Ch. 7], which holds under the mild assumption that the hybrid dynamics satisfy the hybrid basic conditions (these are easily checked for dynamics (39), (46), (58)) and that the attractor is compact (this is easy to verify as well for set $\mathcal{A}$ in (45)). Robustness of asymptotic stability (established in [12, Thm 7.21]) allows to conclude that there exists a sufficiently small, but nonzero perturbation of the dynamics, for which the established nominal asymptotic stability is not destroyed. As a consequence, we expect our control law to perform well also under the presence of uncertainties, such as unmodeled dynamics, or external perturbations, as long as they are sufficiently small, and they are zero when the state belongs to the attractor (see, [12, Ch 7] for details). For more general settings, another useful feature arising from these robustness properties is that for stronger perturbations we have a semiglobal practical robust stability result, established in [12, Thm 7.20]. This result ensures that perturbations not vanishing in $\mathcal{A}$ lead to a gradual deterioration of the convergence properties, which is what one should expect when persistent disturbances, such as atmospheric drag or high solar activities or also measurement noise coming from the GNC devices affect the closed-loop dynamics. All these desirable properties are confirmed by our simulation results of Section V. ○

C. Three-step finite-time control law

The two controllers presented in the previous sections have the following features:

- controller A is desirable because it forces the chaser to evolve along periodic (therefore bounded) motions, but does not lead to a convergence guarantee;
- controller B is desirable because it guarantees finite time convergence, but these maneuvers are fragile since the chaser evolves on divergent trajectory until it reaches its goal. This can be unsafe in case of actuators failure.

In this section we combine the desirable features of the two above laws in a single enhanced control law following again a receding horizon paradigm, arising from the observation that we can separate our control design in two completely decoupled problems corresponding to the following partitions of vectors u and $\widehat{\varepsilon}$:

$$u=\begin{bmatrix}0\\u_y\\0\end{bmatrix}+\begin{bmatrix}1&0\\0&0\\0&1\end{bmatrix}u_{xz}, \quad u_y\in\mathbb{R},\ u_{xz}\in\mathbb{R}^2, \tag{59a}$$

$$\widehat{\varepsilon}=\begin{bmatrix}\widehat{\varepsilon}_y\\\widehat{\varepsilon}_{xz}\\\widehat{\varepsilon}_6\end{bmatrix}, \quad \widehat{\varepsilon}_y\in\mathbb{R}^2,\ \widehat{\varepsilon}_{xz}\in\mathbb{R}^3,\ \widehat{\varepsilon}_6\in\mathbb{R}. \tag{59b}$$

With this partition in mind, we may write the hybrid dynamics of state component $\widehat{\varepsilon}$ in (39) as follows:

$$\begin{cases}\widehat{\varepsilon}_y\,'=0\\ \widehat{\varepsilon}_{xz}\,'=(1-e)^{3/2}\left[\begin{smallmatrix}1\\0\\0\end{smallmatrix}\right]\widehat{\varepsilon}_6 & (\widehat{\varepsilon},\nu,\tau)\in\mathcal{C},\\ \widehat{\varepsilon}_6\,'=0\end{cases} \tag{60a}$$

$$\begin{cases} \widehat{\varepsilon}_y^+ = \widehat{\varepsilon}_y + \hat{B}_y(\nu)u_y \\ \begin{bmatrix} \widehat{\varepsilon}_{xz}^+ \\ \widehat{\varepsilon}_6^+ \end{bmatrix} = \begin{bmatrix} \widehat{\varepsilon}_{xz} \\ \widehat{\varepsilon}_6 \end{bmatrix} + \hat{B}_{xz}(\nu)u_{xz} \end{cases} \quad (\widehat{\varepsilon}, \nu, \tau) \in \mathcal{D}_u, \quad (60b)$$

where

$$\hat{B}_y(\nu) := \frac{1}{k^2\rho}\begin{bmatrix} -s_\nu \\ c_\nu \end{bmatrix}, \quad \hat{B}_{xz}(\nu) := \frac{1}{k^2\rho(1-e^2)} \begin{bmatrix} -e(1+\rho)s_\nu - \frac{3\sigma\rho^2}{(1-e^2)^{3/2}} & \frac{3\sigma e\rho s_\nu}{(1-e^2)^{3/2}} - \rho^2 + \rho + 2 \\ (1-e^2)(1+\rho)s_\nu & (1-e^2)\rho c_\nu \\ (1+\rho)c_\nu + e & -\rho s_\nu \\ -3\rho^2 & 3e\rho s_\nu \end{bmatrix}. \quad (61)$$

Once the dynamics has been separated in two components, we may perform similar computations to (57) and obtain:

$$\widehat{\varepsilon}_y(\mu_2, j_2+1) = \widehat{\varepsilon}_y(\mu_1, j_1) + \underbrace{\begin{bmatrix} \hat{B}_y(\nu_1) & \hat{B}_y(\nu_1+\bar{\nu}) \end{bmatrix}}_{M_y(\nu_1,\bar{\nu}):=} \begin{bmatrix} u_y(\mu_1, j_1) \\ u_y(\mu_2, j_2) \end{bmatrix}, \quad (62)$$

which is simpler than (57) because $\widehat{\varepsilon}_y$ remains constant along flowing solutions. The following result then parallels Conjecture 1 and Lemma 3.

Lemma 4: Given any value of $\bar{\nu} \neq h\pi$, $h \in \mathbb{Z}$, matrix $M_y(\nu, \bar{\nu})$ is nonsingular for all $\nu \in [0, 2\pi]$. Moreover, for any such value of $\bar{\nu}$, selection:

$$u_y := -\begin{bmatrix} 1 & 0 \end{bmatrix} M_y(\nu, \bar{\nu})^{-1} \widehat{\varepsilon}_y, \quad \gamma_\tau(\widehat{\varepsilon}_y, \nu) = \bar{\nu}, \quad (63)$$

guarantees that all solutions to (39), (59), (60) have the $\widehat{\varepsilon}_y$ component equal to zero after at most two jumps.

Proof: Let us first compute:

$$\begin{aligned} \det(M_y(\nu, \bar{\nu})) &= \frac{1}{k^2}\left(\frac{\sin(\nu)\cos(\nu+\bar{\nu})}{\rho(\nu)\rho(\nu+\bar{\nu})} + \frac{\sin(\nu+\bar{\nu})\cos(\nu)}{\rho(\nu)\rho(\nu+\bar{\nu})}\right) \\ &= \frac{\sin(\bar{\nu})}{k^2\rho(\nu)\rho(\nu+\bar{\nu})}, \end{aligned}$$

which proves invertibility of $M_y(\nu, \bar{\nu})$ for all $\bar{\nu} \neq h\pi$, and all ν. The proof of finite-time convergence follows similar steps to the proof of Lemma 3, based on uniqueness of the solution of $\widehat{\varepsilon}_y(\mu_2, j_2+1) = 0$ in (62) and based on the fact that for any solution $\widehat{\varepsilon}_y$ with two consecutive impulses at (μ_1, j_1) and (μ_2, j_2), we have $\widehat{\varepsilon}_y(\mu_2, j_2) = \widehat{\varepsilon}_y(\mu_1, j_1+1)$, due to the trivial flow dynamics in (60a). ∎

Consider now state $\begin{bmatrix} \widehat{\varepsilon}_{xz} \\ \widehat{\varepsilon}_6 \end{bmatrix}$ and input u_{xz}. To obtain periodic motion, from the structure of (60a) and because of Lemma 2, we want to select u_{xz} in such a way that any impulse brings the last component $\widehat{\varepsilon}_6$ of $\widehat{\varepsilon}$ to zero. To this end, paralleling (48a), and with reference to $\hat{B}_{xz}$ in (61), define:

$$\hat{b}_4(\nu) := \frac{3}{k^2(1-e^2)}\begin{bmatrix} -\rho \\ es_\nu \end{bmatrix}, \quad \hat{B}_4^\perp(\nu) := \begin{bmatrix} \frac{es_\nu}{\rho} \\ 1 \end{bmatrix}, \quad (64a)$$

and notice that we may obtain $\widehat{\varepsilon}_6^+ = 0$ with selection:

$$u_{xz} := -\frac{\hat{b}_4(\nu)}{|\hat{b}_4(\nu)|^2}\widehat{\varepsilon}_6 + \hat{B}_4^\perp(\nu) v_{xz}, \quad (64b)$$

which mimics selection (48b), (52). The difference, as compared to before, is that we will now select v_{xz} in (64) following the receding horizon paradigm, which is here simplified because after any impulse, we obtain $\widehat{\varepsilon}_6^+ = 0$ and the solution $\widehat{\varepsilon}_{xz}$ remains constant along flows (see (60a)). Let us then introduce the reduced input matrix:

$$\begin{aligned} \hat{B}_{xz}^r(\nu) &:= \begin{bmatrix} I_3 & 0 \end{bmatrix} \hat{B}_{xz}(\nu)\hat{B}_4^\perp(\nu) \quad (65) \\ &= \frac{1}{k^2\rho^2}\begin{bmatrix} 2 + ec_\nu & 2e + c_\nu(1+e^2) & -s_\nu \end{bmatrix}^\top, \quad (66) \end{aligned}$$

and notice that we need at least three impulses to drive $\widehat{\varepsilon}_{xz}$ to zero. Let us use $\widehat{\varepsilon}_6^+ = 0$ and the arising zero right-hand side of (60a) to obtain that three consecutive impulses with selection (64) lead to (compare to (62)):

$$\widehat{\varepsilon}_{xz}(\mu_3, j_3+1) = \widehat{\varepsilon}_{xz}(\mu_1, j_1) + \underbrace{\begin{bmatrix} \hat{B}_{xz}^r(\nu_1) & \hat{B}_{xz}^r(\nu_1+\bar{\nu}_1) & \hat{B}_{xz}^r(\nu_1+\bar{\nu}_1+\bar{\nu}_2) \end{bmatrix}}_{M_{xz}(\nu_1,\bar{\nu}_1,\bar{\nu}_2):=} \begin{bmatrix} v_{xz}(\mu_1, j_1) \\ v_{xz}(\mu_2, j_2) \\ v_{xz}(\mu_3, j_3) \end{bmatrix}, \quad (67)$$

where $\bar{\nu}_1 = \nu(\mu_2, j_2) - \nu(\mu_1, j_1)$ and $\bar{\nu}_2 = \nu(\mu_3, j_3) - \nu(\mu_2, j_2)$ are the free motions durations between each pair of consecutive impulses. The following result then parallels Lemma 4.

Lemma 5: Given any values of $\bar{\nu}_1$, $\bar{\nu}_2$ such that

$$\bar{\nu}_1 \neq 2h\pi, \quad \bar{\nu}_2 \neq 2h\pi, \quad \bar{\nu}_1 + \bar{\nu}_2 \neq 2h\pi, \quad \forall h \in \mathbb{Z}, \quad (68)$$

matrix $M_{xz}(\nu, \bar{\nu}_1, \bar{\nu}_2)$ is nonsingular for all $\nu \in [0, 2\pi]$. Moreover, selecting any value of $\bar{\nu}_1 = \bar{\nu}_2 = \bar{\nu}$, selection:

$$v_{xz} := -\begin{bmatrix} 1 & 0 & 0 \end{bmatrix} M_{xz}(\nu, \bar{\nu}, \bar{\nu})^{-1} \widehat{\varepsilon}_{xz}, \quad \gamma_\tau(\widehat{\varepsilon}_{xz}, \nu) = \bar{\nu}, \quad (69)$$

guarantees that all solutions to (39), (59), (60), (64) have the $\widehat{\varepsilon}_{xz}$, $\widehat{\varepsilon}_6$ components equal to zero after at most three jumps.

Proof: First consider the following expression that emerges from direct computation:

$$\begin{aligned} d_M &:= \det(M_{xz}(\nu, \bar{\nu}_1, \bar{\nu}_2)) \\ &= 2\frac{\sin(\bar{\nu}_1) + \sin(\bar{\nu}_2) - \sin(\bar{\nu}_1+\bar{\nu}_2)}{\rho(\nu)^2\rho(\nu+\bar{\nu}_1)^2\rho(\nu+\bar{\nu}_1+\bar{\nu}_2)^2}. \end{aligned} \quad (70)$$

since ρ never vanishes we may study the invertibility of M_{xz} by only focusing on the numerator, which satisfies:

$$\begin{aligned} d_M^n &= \sin(\bar{\nu}_1) + \sin(\bar{\nu}_2) - \sin(\bar{\nu}_1+\bar{\nu}_2) \\ &= \sin(\bar{\nu}_1)(1-\cos(\bar{\nu}_2)) + \sin(\bar{\nu}_2)(1-\cos(\bar{\nu}_1)) \\ &= 4\sin\left(\frac{\bar{\nu}_1}{2}\right)\sin\left(\frac{\bar{\nu}_2}{2}\right)\sin\left(\frac{\bar{\nu}_1}{2}+\frac{\bar{\nu}_2}{2}\right) \end{aligned} \quad (71)$$

and which clearly does not vanish if and only if (68) holds, regardless the value of ν.

The fact that with controller (69) all solutions have $\widehat{\varepsilon}_{xz}$, $\widehat{\varepsilon}_6$ converge to zero in finite time follows similar steps to the proof of Lemma 4, from uniqueness of v_{xz} in (69). ∎

The following result can be established by similar derivations to those in the proof of Theorem 2, relying on the uniform finite-time convergence established in Lemmas 4 and 5. Its proof is omitted due to this similarity to that of Theorem 2.

Theorem 3: Control law (59), (63), (64b), (69) ensures that attractor $\mathcal{A}$ in (45) is uniformly globally asymptotically stable along the closed-loop dynamics with (39).

Figure 3 shows the level sets of $\det(M_{xz}(\nu, \bar{\nu}_1, \bar{\nu}_2))$, which clearly indicates that the determinant is maximized with $\bar{\nu}_1 = \bar{\nu}_2 = 120°$. Due to this fact and to reduce consumption, we select this value for $\bar{\nu}_1 = \bar{\nu}_2$ in our simulation section.

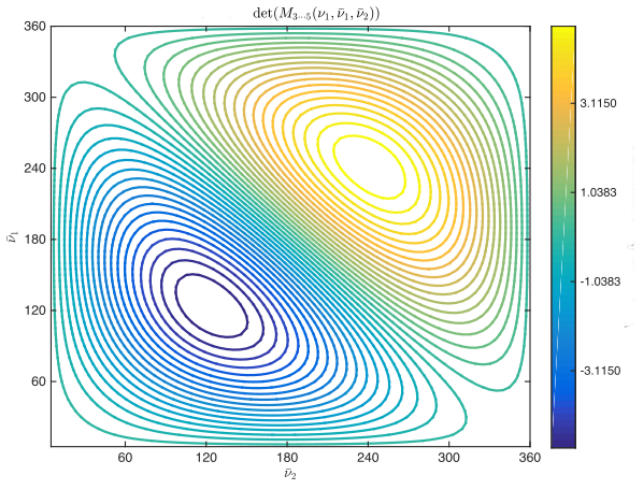

Fig. 3: Level sets for $\det(M_{xz}(\nu, \bar{\nu}_1, \bar{\nu}_2))$.

Remark 3: The three control laws proposed in this section require estimates of relative positions and velocities of the follower. During proximity operations, far range and close range rendezvous operations, relative measurements of positions and velocities between the leader and the follower may be provided either by passive or active sensors data processed by the navigation system of the follower (e.g. vision-based relative pose estimation, filtered Carrier-phase Differential GPS) [10]. Note that the impact of the sensors noise and the robustness of the hybrid schemes are analyzed numerically in the simulation section and are expected to be non-damageful for the asymptotically stable closed loops in light of the robustness results highlighted in Remark 2. ◦

V. Simulations

In this section, we present the simulation results obtained with the control laws designed in Section IV and system (39) (equivalently (41)–(43)) using a nonlinear simulator and comparing the results with a linearized model in *Matlab-Simulink* for the PRISMA mission [5].

A. Simulated context and performance metrics

The simulator is composed by two main blocks: the controller and the dynamics. The controller recovers the current state in LVLH coordinates and transforms it into state $\widehat{\xi}$ to compute the mismatch (37). Afterwards, the control input u is computed, to be applied to the dynamics block.

For a given orbital rendezvous scenario, the output of the nonlinear simulator is the history of the relative position and velocity between the two spacecrafts, obtained by simulating their inertial trajectories in the Earth-centered frame via the integration of the Gauss equations. The simulator accounts for the disturbances provoked by the Earths oblatness (so-called J_2-effect) and the atmospheric drag. Moreover, uncertainties that originate from GNC devices (measurement noise and chemical thrusters limitations) are also simulated. For instance, the measured relative state is affected by a white noise characterised by the following standard deviation on the relative position and velocity: $d_p = 10^{-2}$ m, $d_v = 10^{-5}$ m/s (see Remark 3). Then, the applied control u is obtained from the computed control u^* through the thrusters saturation and dead-zone filter along each axis independently:

$$u_i = \begin{cases} u_i^* \text{ if } u_i^* \in [-\Delta v_{max} \ -\Delta v_{min}] \ \cup \ [\Delta v_{min} \ \Delta v_{max}], \\ 0 \text{ if } u_i^* \in [-\Delta v_{min} \ \Delta v_{min}], \\ \dfrac{u_i^*}{|u_i^*|}\Delta v_{max} \text{ if } u_i^* \in (-\infty \ -\Delta v_{max}] \ \cup \ [\Delta v_{max} \ \infty), \end{cases} \tag{72}$$

with $\Delta v_{max} = 0.5$ m/s and $\Delta v_{min} = 5 \cdot 10^{-4}$ m/s. This simulation set-up is a simple way to check the robustness properties of hybrid schemes mentioned in Remark 2. Aside, a linearized dynamics with no environment disturbances nor devices uncertainties is also propagated along with the different controllers for the sake of comparison.

Within the PRISMA mission, the leader vehicle evolves on a given orbit with a semi-major axis of 7011 km, an eccentricity of $e = 0.004$ and an inclination of $i = 98$ deg. The performed simulations are run from the initial true anomaly $\nu_0 = 0$ up to a final true anomaly $\nu_f = \nu_0 + 20\pi$, namely ten orbital periods later. The chaser satellite begins the rendezvous maneuver at initial state X_0 at $\nu_0 = 0$. The simulations aim at stabilizing the chaser in a periodic trajectory specified by a suitable selection of $\widehat{\xi}^{\,ref}$ in (36):

$$\widehat{\xi}^{\,ref} = \begin{bmatrix} 7.68 & 17.68 & 87.78 & 33.04 & -15.77 & 0 \end{bmatrix}^T \tag{73}$$

where we emphasize that the last element is zero (a necessary and sufficient condition for periodic motion, as established in Lemma 2). The reference periodic trajectory $\widehat{\xi}^{\,ref}$ is free to evolve inside a tolerance box $\mathcal{B}$, centered at point $X_{\mathcal{B}} = [100 \ 0 \ 0]^T$ m (expressed in the target's position frame used in (1)) and has positive and negative widths $X_{tol} = [50 \ 25 \ 25]^T$ m in the three LVLH directions.The different control thrusts are separated by an angular distance $\bar{\nu} = 120°$ from one to another along the whole duration of the rendezvous. This value of $\bar{\nu}$ has been selected in order to maximize the norm of the determinant of matrix M either from (57) or (67) depending on the selected control law (see Figures 2 and 3). Doing this, the consumption is expected to be reduced as the control input is computed through the inversion of M.

For each one of the three control laws in Section IV, four different initial conditions X_{0i}, $i = 1, \cdots, 4$ for state $X(t)$ in (1) have been used, which are chosen at four different distances from the target satellite located at the origin of the LVLH frame:

$$\begin{aligned} |X_{01}| &\approx 500, \text{ m} & |X_{02}| &\approx 750, \text{ m} \\ |X_{03}| &\approx 2000, \text{ m} & |X_{04}| &\approx 5200 \text{ m}. \end{aligned}$$

The initial conditions are selected as:

$$\begin{aligned} X_{01} &= \begin{bmatrix} 400 & 300 & -40 & 0 & 0 & 0 \end{bmatrix}^T, \\ X_{02} &= \begin{bmatrix} 600 & 400 & 200 & 0 & 0 & 0 \end{bmatrix}^T, \\ X_{03} &= \begin{bmatrix} -1500 & 1300 & 150 & 0 & 0 & 0 \end{bmatrix}^T, \\ X_{04} &= \begin{bmatrix} 5000 & 1300 & 500 & 0 & 0 & 0 \end{bmatrix}^T, \end{aligned} \tag{74}$$

where the first three components are meters and the last three are meters per second. Let us denote by $\widehat{\xi}_{0i}$ the image of the initial states X_{0i} through $R(\nu)$ defined in (34). The initial

relative velocity has been selected to be zero to account for the fact that the starting point of our trajectory may be a holding point arising from a previous station keeping along the space mission.

Two performance indexes are considered: the fuel consumption J, and the convergence time T_c, both described next.

The fuel consumption is characterized in [19] when firing is achieved by 6 identical thrusters rigidly mounted to the satellite, and corresponds to the cost function:

$$J := \sum_{\nu_k \in \mathcal{V}} \|u(\nu_k)\|_1, \tag{75}$$

where $u = \Delta\nu$ has been introduced in (5), (7), $\mathcal{V}$ is the set of firing instants, and $|\cdot|_1$ denotes the 1-norm, so that $\|\Delta v(\nu_k)\|_1 = |\Delta v_x(\nu_k)| + |\Delta v_y(\nu_k)| + |\Delta v_z(\nu_k)|$. The convergence is evaluated by means of the mismatch ratio η given by

$$\eta(\nu) = \frac{\|\widehat{\varepsilon}(\nu)\|_2}{\|\widehat{\varepsilon}(\nu_0)\|_2} = \frac{\|\widehat{\xi}(\nu) - \widehat{\xi}^{\,ref}\|_2}{\|\widehat{\xi}(\nu_0) - \widehat{\xi}^{\,ref}\|_2} \tag{76}$$

The convergence time T_c is defined as the smallest time after which the solution remains in the δ vicinity of the reference point, namely:

$$\eta(\nu) \leq \delta, \quad \forall\, \nu \geq T_c \tag{77}$$

where δ is set to 5%.

B. Comparative simulation results

Different simulations have been performed for each one of the three control laws in Section IV, and for each one of the initial conditions in (74). The trajectories concerning the initial condition X_{01} for the three controllers are represented in Figures 4, 5 and 6. The applied impulses and the convergence profile are represented in Figures 7, 8 and 9. The trajectories from the other initial conditions have not been included for sake of brevity.

In the following study, we first address the results of the linear simulations in order to analyze the nominal behavior of the different controllers. Then, we focus on the nonlinear simulation to assess their robustness with respect to modeling errors, navigation uncertainties and input saturation. Finally, for the sake of comparison, we report on the simulation results obtained with the MPC controller proposed in [11].

Linear simulations. Figures 7, 8 and 9 reveal how the different control strategies steer the chaser to the tolerance box along different paths in a linear environment. Controller IV-A makes the chaser inch to the tolerance box while controllers IV-B and IV-C have more "straight" paths. These facts are corroborated by the impulsive control plan on the upper graphs of Figures 7, 8 and 9. Controllers IV-B and IV-C concentrate most of their consumption on the two first controls while the 7 first controls have a relative importance for controller IV-A.

The differences among the control strategies can also be observed on the evolution of η the mismatch ratio (lower graphs of Figures 7, 8 and 9). Thanks to the safe orbit transfer philosophy (maintaining $\widehat{\xi}_6$ to zero which ensures, by Lemma 2, intermediate periodic motions), the controllers IV-A and IV-C make the tracking trajectory jump from a periodic orbit to another so that $\widehat{\xi}$ and $\widehat{\varepsilon}$ remain constant between control impulses. On the contrary, controller IV-B allows to follow a path possibly with a high divergence coefficient $\widehat{\xi}_6$, so that the error norm can possibly evolve fast (either diverging or converging) between successive firing times. Indeed, in the linear simulation, controller IV-B provides faster convergence time, compared to controllers IV-A and IV-C, with an equivalent consumption. In fact, in an ideal context, only two impulses are needed to bring the chaser to the steady state, while IV-A and IV-C need at least four impulsive controls. On the other hand, if controller IV-A is the slowest in the linear simulator, it is generally the less demanding in terms of consumption among the hybrid controllers, as expected.

Nonlinear simulations. Addressing the nonlinear simulations, two cases can be distinguished depending on how close to the target relative orbit the chaser starts. For the close range control maneuvers (starting from initial conditions X_{01}) illustrated in Figures from 4 to 9, the difference between the linear and nonlinear simulations are slight: the consumption and the convergence time are equivalent, as one can notice from the first rows of Tables I and II.It can also be observed on figures 7, 8 and 12 that no controls are saturated: the feedback control is properly executed in close range in the nonlinear simulation. However, the trajectories have small differences that can be imputed to the dynamics linearization process and navigation uncertainties. Analyzing the simulations starting from the initial states X_{02}, the same kind of conclusions can be drawn. Note that for controllers IV-A and IV-C, the control inputs are slightly saturated but not enough to degrade the performances in terms of convergence time.

On the contrary the simulations from the initial states X_{03} and X_{04} expose different behaviors. Due to the larger distance from the box, every controllers demand for a first large impulsive control action. However, it can be observed on Figures 10, 11 and 12 that all these first impulses are saturated in the nonlinear simulator. Each controller reacts in a different manner to such a drawback. Controller IV-B fails to stabilize the chaser in the presence of saturations for initial states X_{03} and X_{04}. In fact, the size of input $u = \Delta v$ (see (5) and (7)) demanded by the controller is largely beyond the thrusters capabilities, while such an amount is supposed to steer the chaser to the box after two impulses. Instead, since the impulsive controls are truncated, the chaser is brought on a random orbit with no particular interest and obviously divergent (see Figure 11). On the contrary, for controllers IV-A and IV-C, a part of the control is dedicated to guiding the chaser to the set of periodic orbits. Thus, even if this control is truncated, the chaser is steered to states with gradually decreasing divergence parameter $\widehat{\xi}_6$. This fact can be observed on Figures 10 and 12, where the slope of the error norm decreases after each impulsive control and tends to zero. Both controllers expose two phases: first stabilizing $\widehat{\xi}_6$ and then steering states ξ_1 to ξ_5 to ξ^{ref}. The consequence is that the convergence time is degraded for both controllers. Naturally, the presence of saturation limits the consumption for both controllers, as compared to the linear simulations. Indeed controllers IV-A and IV-C show some robustness abilities with

respect to saturation at the price of a slower convergence time.

Comparison with MPC strategy. Parallel simulations have been performed with the MPC-based method recently presented in [11], which directly addresses the minimization of J and accounts for saturation. This controller has been benchmarked using the nonlinear simulator. For the sake of comparison, we report on the controlled trajectory for the initial condition X_{01}, shown in Figure 13, and the applied impulses as well as the profile of η, shown in Figures 14 and 15 for the initial conditions X_{01} and X_{04}. Note that in the MPC framework η refers to the relative distance from the set of the relative periodic orbits included in the tolerance box (see [9] for a rigorous description of this set) including the relative orbit ξ^{ref}.

For the close range initial conditions (X_{01} and X_{02}), the hybrid controllers ensure faster convergence of the chaser as compared to the MPC controller. This can be explained by two facts. First, it has been mentioned earlier that, for those initial conditions, the behavior of the hybrid controllers is equivalent between the nonlinear and the linear simulator, probably due to the fact that saturation does not play a dominant role. Second, the convergence and stability properties of the hybrid controllers probably justifies the faster convergence as compared to the MPC controller from [11], which lacks a guarantee of asymptotic stability.

For the initial conditions X_{03} and X_{04}, the performance of the hybrid controllers are degraded probably because of the saturations. Conversely the MPC controller, which explicitly takes into account the presence of saturations, exhibits a better behavior for far range initial conditions. Finally, using the MPC controller leads to smaller consumption at the price of a significantly higher numerical complexity (a numerical optimization must be solved at each firing instant).

VI. Conclusions

In this article, a new model, based on Floquet-Lyapunov theory, is developed in order to obtain a linear time-invariant free motion representation of the rendezvous problem. This problem is then recast as a stabilization problem for a periodic trajectory in a hybrid dynamical system framework. Two new control laws have been proposed and compared to a control scheme given in [8], which is re-interpreted in this hybrid context.

The new controllers take the advantage of steering the satellite motion along periodic (therefore bounded) transient relative orbits. The use of the hybrid formalism allows us to prove asymptotic stability of the desired motion, in addition to robustness to perturbations. Such a robustness is confirmed by suitable simulation results showing desirable responses also in the presence of unmodeled nonlinear phenomena and external disturbances affecting the satellite motion.

Initial	Control A		Control B		Control C		MPC
condition	LIN	NL	LIN	NL	LIN	NL	NL
X_{01}	1.00	1.10	0.86	1.10	0.93	1.02	0.57
X_{02}	1.92	1.92	2.18	2.19	2.85	2.40	1.37
X_{03}	4.50	3.77	4.44	$\times\times\times$	4.00	4.12	2.17
X_{04}	9.05	8.96	9.23	$\times\times\times$	9.35	8.16	7.11

TABLE I: Consumption J (m/s).

Initial	Control A		Control B		Control C		MPC
condition	LIN	NL	LIN	NL	LIN	NL	NL
X_{01}	2.91	2.86	0.34	0.34	0.98	0.97	1.63
X_{02}	2.59	2.59	0.34	0.34	0.98	0.98	1.34
X_{03}	3.55	2.91	0.34	$\times\times\times$	0.98	1.94	1.64
X_{04}	3.87	5.48	0.33	$\times\times\times$	0.98	4.20	2.97

TABLE II: Convergence time T_c (nb. orbits).

References

[1] K.T. Alfriend and H. Schaub. Dynamics and control of spacecraft formations: Challenges and some solutions. *Journal of the Astronautical Sciences*, 48(2):249–267, 2000.

[2] K.T. Alfriend, S.R. Vadali, P. Gurfil, J.P. How, and L.S. Breger. *Spacecraft Formation Flying*. elsevier, Burlington, MA, USA, 2010.

[3] A. Ben-Israel and T. NE Greville. *Generalized inverses: theory and applications*, volume 15. Springer Science & Business Media, 2003.

[4] S. Bittanti and P. Colaneri. *Periodic Systems: Filtering and Control*. Communications and Control Engineering. Springer, 2008.

[5] P. Bodin, R. Larsson, F. Nilsson, C. Chasset, R. Noteborn, and M. Nylund. Prisma: an in-orbit test bed for guidance, navigation, and control experiments. *Journal of Spacecraft and Rockets*, 46(3):615–623, 2009.

[6] M. Brentari, D. Arzelier, C. Louembet, L.S. Urbina, and L. Zaccarian. A hybrid control framework for impulsive control of satellite rendezvous. In *American Control Conference*, Boston (MA), USA, July 2016.

[7] G. Deaconu, C. Louembet, and A. Theron. Constrained periodic spacecraft relative motion using non-negative polynomials. In *American Control Conference (ACC), 2012*, June 2012.

[8] G. Deaconu, C. Louembet, and A. Theron. A two-impulse method for stabilizing the spacecraft relative motion with respect to a periodic trajectory. In *Decision and Control (CDC), 2012 IEEE 51st Annual Conference on*, Dec 2012.

[9] G. Deaconu, C. Louembet, and A. Théron. Designing continuously constrained spacecraft relative trajectories for proximity operations. *Journal of Guidance, Control, and Dynamics*, 38(7):1208–1217, 2015.

[10] W. Fehse, editor. *Automated rendezvous and docking of spacecraft*. Cambridge Aerospace Series. Cambridge University Press, Cambridge, UK, 2003.

[11] Paulo Ricardo Arantes Gilz, Mioara Joldes, Christophe Louembet, and Frdric Camps. Model predictive control for rendezvous hovering phases based on a novel description of constrained trajectories. *IFAC-PapersOnLine*, 50(1), 2017. 20th IFAC World Congress.

[12] R. Goebel, R.G. Sanfelice, and A.R. Teel. *Hybrid Dynamical Systems: modeling, stability, and robustness*. Princeton University Press, 2012.

[13] P. Gurfil. Relative motion between elliptic orbits: Generalized boundedness conditions and optimal formationkeeping. *Journal of Guidance, Control and Dynamics*, 28(4):761–767, July 2005.

[14] G. Inalhan, M. Tillerson, and J.P. How. Relative dynamics and control of spacecraft formations in eccentric orbits. *Journal of Guidance, Control and Dynamics*, 25(1):48–59, January-February 2002.

[15] C. Jewison and R.S. Erwin. A spacecraft benchmark problem for hybrid control and estimation. In *Decision and Control (CDC), 2012 IEEE 51st Annual Conference on*, Las Vegas, Nevada, USA, Dec 2016.

[16] D.F. Lawden. *Optimal trajectories for space navigation*. Butterworth, London, England, 1963.

[17] C. Louembet, D. Arzelier, and G. Deaconu. Robust rendezvous planning under maneuver execution errors. *Journal of Guidance, Control, and Dynamics*, 2015.

[18] B.P. Malladi, R.G. Sanfelice, E. Butcher, and J. Wang. Robust hybrid supervisory control for rendezvous and docking of a spacecraft. In *Decision and Control (CDC), 2012 IEEE 51st Annual Conference on*, Las Vegas, Nevada, USA, Dec 2016.

[19] I.M. Ross. 6 space trajectory optimization and l 1-optimal control problems. *Elsevier Astrodynamics Series*, 1:155–VIII, 2007.

[20] H. Schaub. Relative orbit geometry through classical orbit element differences. *Journal of Guidance, Control, and Dynamics*, 2004.

[21] P. Sengupta and S.R. Vadali. Relative motion and the geometry of formations in keplerian elliptic orbits. *Journal of Guidance, Control, and Dynamics*, 2007.

[22] R.E. Sherill, A.J. Sinclair, T.A. Lovell, and S.C. Sinha. Lyapunov-floquet transformation of satellite relative motion in elliptic orbits. *Celestial Mechanics and Dynamical Astronomy*, 119:55–73, 2014.

[23] J. Tschauner. The elliptic orbit rendezvous. In *AIAA 4th Aerospace Sciences Meeting*, Los Angeles, Californie, USA, Juin 1966.

[24] K. Yamanaka and F. Ankersen. New state transition matrix for relative motion on an arbitrary elliptical orbit. *Journal of Guidance, Control, and Dynamics*, 25(1):60–66, January 2002.

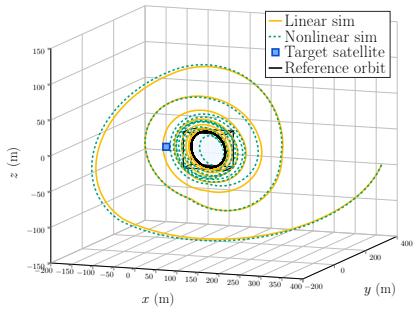

Fig. 4: Trajectories for controller A when starting from X_{01}.

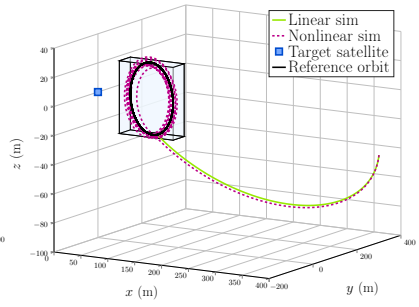

Fig. 5: Trajectories for controller B when starting from X_{01}.

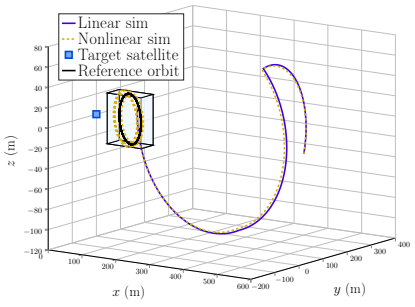

Fig. 6: Trajectories for controller C when starting from X_{01}.

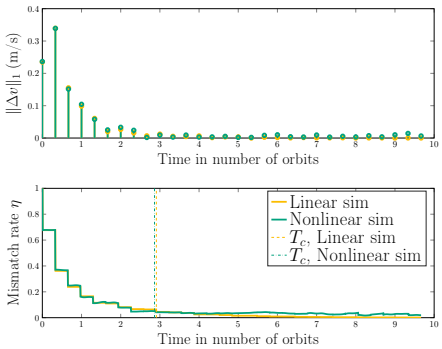

Fig. 7: Impulses and convergence from X_{01} for controller A.

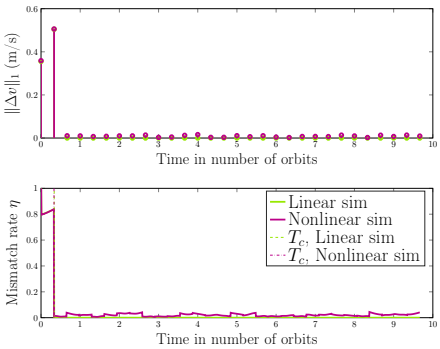

Fig. 8: Impulses and convergence from X_{01} for controller B.

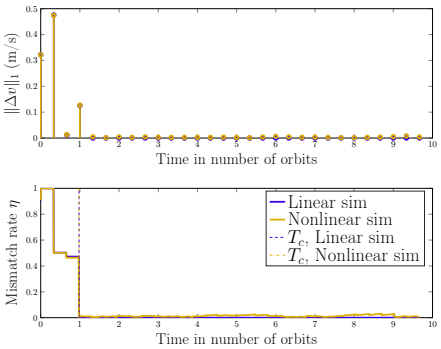

Fig. 9: Impulses and convergence from X_{01} for controller C.

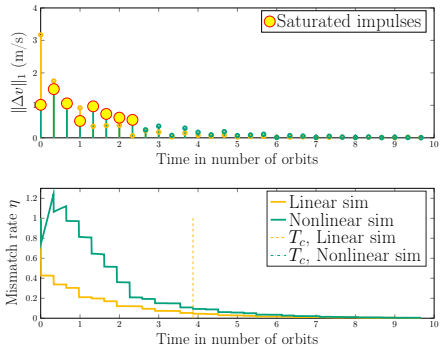

Fig. 10: Impulses and convergence from X_{04} for controller A.

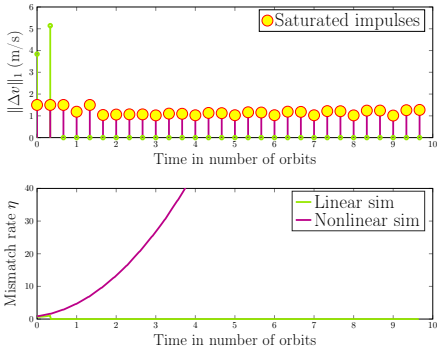

Fig. 11: Impulses and convergence from X_{04} for controller B.

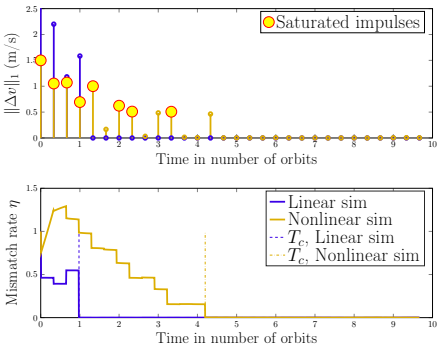

Fig. 12: Impulses and convergence from X_{04} for controller C.

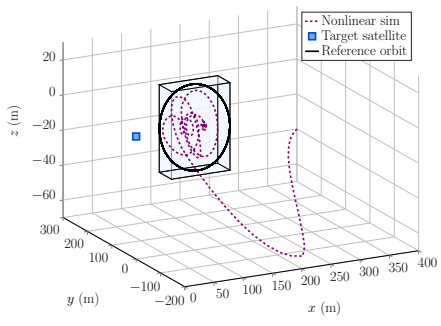

Fig. 13: Trajectory for the MPC controller when starting from X_{01}.

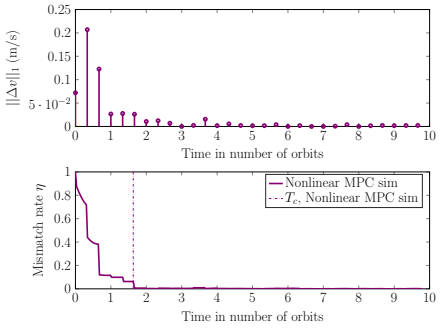

Fig. 14: Impulses and convergence from X_{01} for the MPC controller.

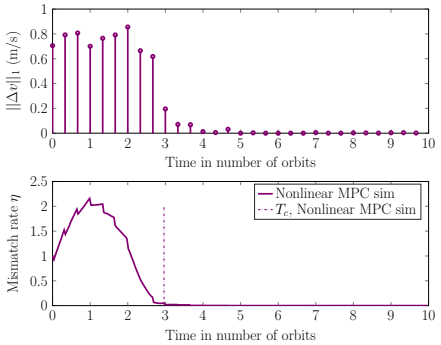

Fig. 15: Impulses and convergence from X_{04} for the MPC controller.